Supplementary Information for

On-demand Photonic Ising Machine with Simplified Hamiltonian Calculation by Phase Encoding and Intensity Detection

Jiayi Ouyang[1], Yuxuan Liao[1], Zhiyao Ma[1], Deyang Kong[1], Xue Feng[1]*, Xiang Zhang[2], Xiaowen Dong[2], Kaiyu Cui[1], Fang Liu[1], Wei Zhang[1], and Yidong Huang[1]

[1]Department of Electronic Engineering, Tsinghua University, Beijing 100084, China
[2]Central Research Institute, Huawei Technologies Co. Ltd., Shenzhen, 518129, China
*Correspondence: x-feng@tsinghua.edu.cn

This file includes:

Supplementary Notes 1 to 7
Supplementary Figures 1 to 9
Supplementary Tables 1 to 5
Supplementary References

Supplementary Note 1: Detailed deduction in the pretreatment stage and the measurement of the experimental Hamiltonian

At first, we would like to introduce the principle of solving an Ising problem with our proposed Phase Encoding and Intensity Detection Ising Annealer (PEIDIA). in detail. For a given N-spin Ising model, we first decompose the adjacent interaction matrix $\mathbf{J}$ to the symmetric matrix $\mathbf{J}_+ = (\mathbf{J} + \mathbf{J}^\mathrm{T})/2$ (the superscript T denotes the transpose) and the anti-symmetric matrix $\mathbf{J}_- = (\mathbf{J} - \mathbf{J}^\mathrm{T})/2$. As $\mathbf{J}_-$ does not contribute to the Hamiltonian, we use $\mathbf{J}$ to denote the symmetric component $\mathbf{J}_+$ for simplicity. Thus, the real symmetric matrix $\mathbf{J}$ can be decomposed with eigen-decomposition[1],

$$\mathbf{J} = \mathbf{Q}^\mathrm{T}\mathbf{D}\mathbf{Q}, \tag{S1}$$

where the $\mathbf{D} = \mathrm{diag}(\lambda_1, \lambda_2, \dots, \lambda_N)$ is the diagonal eigenvalue matrix with N eigenvalues $\lambda_1, \lambda_2, \dots, \lambda_N$, and $\mathbf{Q}$ is the corresponding normalized orthogonal eigenvector matrix. By introducing $\mathbf{A} = \sqrt{\mathbf{D}}\mathbf{Q}$:

$$\mathbf{J} = \mathbf{Q}^\mathrm{T}\sqrt{\mathbf{D}}\sqrt{\mathbf{D}}\mathbf{Q} = \mathbf{A}^\mathrm{T}\mathbf{A}. \tag{S2}$$

With such decomposition, the Ising Hamiltonian H can be written as

$$H(\boldsymbol{\sigma}) = -\frac{1}{2}\sum_{1\le i,j\le N} J_{ij}\,\sigma_i\sigma_j = -\frac{1}{2}\boldsymbol{\sigma}^\mathrm{T}\mathbf{J}\boldsymbol{\sigma} = -\frac{1}{2}(\mathbf{A}\boldsymbol{\sigma})^\mathrm{T}(\mathbf{A}\boldsymbol{\sigma}), \tag{S3}$$

where $\boldsymbol{\sigma} = [\sigma_1, \sigma_2, \dots, \sigma_N]^\mathrm{T}$ $(\sigma_i \in \{-1,1\})$ denotes the Ising spin vector. In Eq. (S3), the Hamiltonian is the product of the transformed spin vector $\mathbf{A}\boldsymbol{\sigma}$ and its transpose. It should be mentioned that the eigenvalues $\lambda_1, \lambda_2, \dots, \lambda_N$ may be negative. For convenience, suppose that $\boldsymbol{J}$ has k negative eigenvalues that satisfies $\lambda_1 \le \lambda_2 \le \dots \le \lambda_k < 0 \le \lambda_{k+1} \le \dots \le \lambda_N$. Thus, the square root of the diagonal eigenvalue matrix $\mathbf{D}$ can be expressed as $\sqrt{\mathbf{D}} = \mathrm{diag}(\mathrm{i}\sqrt{-\lambda_1}, \mathrm{i}\sqrt{-\lambda_2}, \dots \mathrm{i}\sqrt{-\lambda_k}, \sqrt{\lambda_{k+1}}, \dots, \sqrt{\lambda_N})$. As $\mathbf{Q} = \{q_{ij}\}$ is a real matrix, the transformation matrix $\mathbf{A}$ has the following form

$$\mathbf{A} = \begin{bmatrix} \mathrm{i}\sqrt{-\lambda_1}q_{11} & \cdots & \mathrm{i}\sqrt{-\lambda_1}q_{k1} & \mathrm{i}\sqrt{-\lambda_1}q_{1,k+1} & \cdots & \mathrm{i}\sqrt{-\lambda_1}q_{1N} \\ \vdots & \ddots & \vdots & \vdots & \ddots & \vdots \\ \mathrm{i}\sqrt{-\lambda_k}q_{k1} & \cdots & \mathrm{i}\sqrt{-\lambda_k}q_{k,k} & \mathrm{i}\sqrt{-\lambda_k}q_{k,k+1} & \cdots & \mathrm{i}\sqrt{-\lambda_k}q_{kN} \\ \sqrt{\lambda_{k+1}}q_{k+1,1} & \cdots & \sqrt{\lambda_{k+1}}q_{k+1,k} & \sqrt{\lambda_{k+1}}q_{k+1,k+1} & \cdots & \sqrt{\lambda_{k+1}}q_{k+1,N} \\ \vdots & \ddots & \vdots & \vdots & \ddots & \vdots \\ \sqrt{\lambda_N}q_{N,1} & \cdots & \sqrt{\lambda_N}q_{N,k} & \sqrt{\lambda_N}q_{N,k+1} & \cdots & \sqrt{\lambda_N}q_{N,N} \end{bmatrix}, \tag{S4}$$

where the first k rows are imaginary, while the rest $(N-k)$ rows are real. Similarly, since the spin vector $\boldsymbol{\sigma}$ is also real, the first k elements of the transformed spin vector $\mathbf{E} = \mathbf{A}\boldsymbol{\sigma}$ are imaginary while the rest elements are real. Thus it can be written as $\mathbf{E} = \mathbf{A}\boldsymbol{\sigma} = [\mathrm{i}e_1 \quad \dots \quad \mathrm{i}e_k \quad e_{k+1} \quad \dots \quad e_N]^\mathrm{T}$ $(e_i \in \mathbb{R})$. In the PEIDIA, the optical vector-matrix multiplication (OVMM) is set to $\mathbf{A}$ and the input vector is set to $\boldsymbol{\sigma}$. Since only the intensity of the light field can be detected, the output intensity vector is

$$\mathbf{I} = \mathbf{E}^* \odot \mathbf{E} = [e_1^2 \quad \dots \quad e_k^2 \quad e_{k+1}^2 \quad \dots \quad e_N^2]^\mathrm{T} = [I_1 \quad \dots \quad I_k \quad I_{k+1} \quad \dots \quad I_N]^\mathrm{T}, \tag{S5}$$

where $\odot$ denotes element-wise multiplication. Thus Eq. (S3) can be further rewritten as

$$H(\boldsymbol{\sigma}) = -\frac{1}{2}\mathbf{E}^\mathrm{T}\mathbf{E} = (I_1 + I_2 + \dots + I_k - I_{k+1} - \dots - I_N)/2. \tag{S6}$$

Then the relation between the measured intensities and the corresponding Hamiltonian is

$$H = -\frac{1}{2}\boldsymbol{\sigma}^\mathrm{T}\mathbf{J}\boldsymbol{\sigma} = \frac{1}{2}\left(\sum_{i,\,\lambda_i<0} I_i - \sum_{i,\,\lambda_i>0} I_i\right). \tag{S7}$$

In conclusion, in the pretreatment stage, the required optical transformation matrix $\mathbf{A}$ is obtained by the eigen-decomposition of the Ising interaction matrix $\mathbf{J}$. The experimental Hamiltonian can be calculated from the output intensities of the OVMM. In the main text, a 20-spin antiferromagnetic Möbius-Ladder model (model 1) and two randomly generated, fully connected spin-glass models (model 2 and 3 with 20 and 30 spins respectively) are demonstrated, and their interaction matrices $\mathbf{J}$ and corresponding transformation matrices $\mathbf{A}$ are shown in Supplementary Figure 1 respectively.

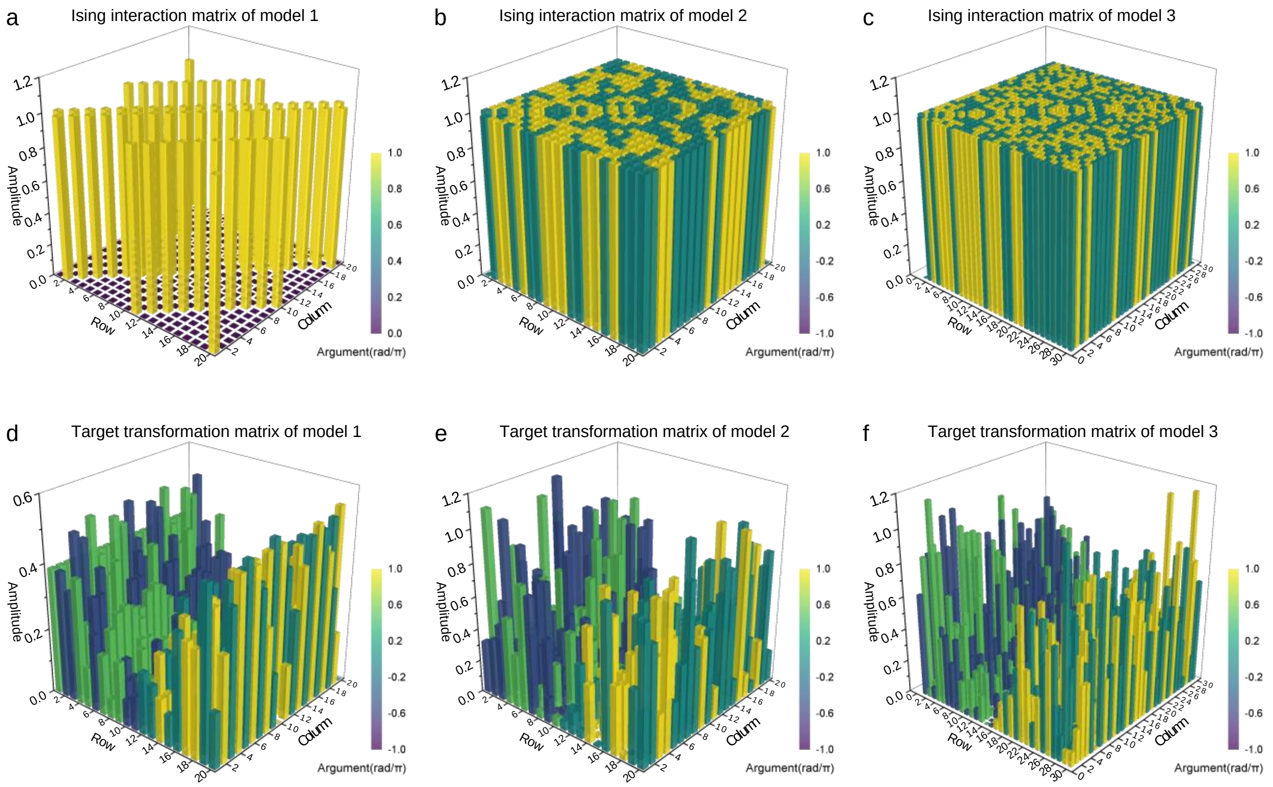

Supplementary Figure 1. Related matrices of model 1-3. (a)-(c) The Ising interaction matrices of model 1-3 respectively. (d)-(f) The target transformation matrices $\mathbf{A}$ of model 1-3 respectively.

Supplementary Note 2: Full operation process of the PEIDIA

The operation principle of PEIDIA is modified from the simulated annealing algorithm[2,3] and inspired by the fast simulated annealing algorithm[4]. The process of each run is:

Input**:** Ising interaction matrix $\mathbf{J}$, number of spins N, transformation matrix $\mathbf{A}$, initial random spin vector $\boldsymbol{\sigma}^{(0)}$, initial Hamiltonian $H^{(0)}$, initial annealing temperature T_0, steps per temperature n_{step}, stages of the temperature n_{temp}, annealing coefficient η, Cauchy scaling coefficient α.

Output**:** $\boldsymbol{\sigma}$

Initialization: annealing temperature: $T \leftarrow T_0$, Hamiltonian: $H \leftarrow +\infty$, spin vector: $\boldsymbol{\sigma} \leftarrow \boldsymbol{\sigma}^{(0)}$, patterns on SLMs: calibrated patterns corresponding to $\mathbf{A}$.

For $i = 1$ to n_{temp} do

For $j = 1$ to n_{step} do

Generate a Cauchy random variable $x \sim C(x; 0, \alpha T)$ until $m = \text{round}(|x|) < N$

If $m = 0$

$m \leftarrow 1$

Else if $m > N/2$

$m \leftarrow N - m$

End if

Generate the spin state $\boldsymbol{\sigma}_{\text{next}}$ by randomly flip m spins from $\boldsymbol{\sigma}$

Update SLM1 according to $\boldsymbol{\sigma}_{\text{next}}$

Calculate H_{next} according to the measured beam intensities

If $H_{\text{next}} < H$ or rand(0,1)<exp$\left(-\frac{H_{\text{next}}-H}{T}\right)$

$\boldsymbol{\sigma} \leftarrow \boldsymbol{\sigma}_{\text{next}}$

$H \leftarrow H_{\text{next}}$

End if

End for

$T \leftarrow \eta T$

End for

Return $\boldsymbol{\sigma}$

Supplementary Note 3: Experimental demonstration of the PEIDIA

The experimental setup is illustrated in Supplementary Figure 2. The whole system is placed on an optical table with vibration isolators and covered by a glass cabinet while the temperature of the laboratory is also kept constant. The operating wavelength of the laser (ORION 1550nm Laser Module) is 1550nm. Each employed reflective phase-only SLM (HOLOEYE PLUTO-2.1-TELCO-013) has 1920×1080 pixels with the pixel pitch of 8μm. The distance between SLM0 and SLM1 is L_{01}=0.820m. The distance between SLM1 and SLM2 is L_{12}=0.754m. The distance between SLM2 and pinhole is $L_{2\text{p}}$=0.373m. The final output field is measured by the Hamamatsu InGaAs C12741-03 camera. To weaken the influence of the detection noise, the measured image of each sampled state is the average of 3 adjacent frames. Supplementary Figure 3 shows the experimentally utilized SLM patterns for model 2 as an example. Supplementary Figure 3a is the beam-splitting pattern on SLM0. 20 beam-splitting and beam-recombining circular regions are shown in Supplementary Figures 3b and 3c respectively with the radius of each region is 1175μm. Supplementary Figure 4 shows the SLM1 pattern used in the experiment of model 3, which contains 30 beam-splitting regions with radius of 950μm.

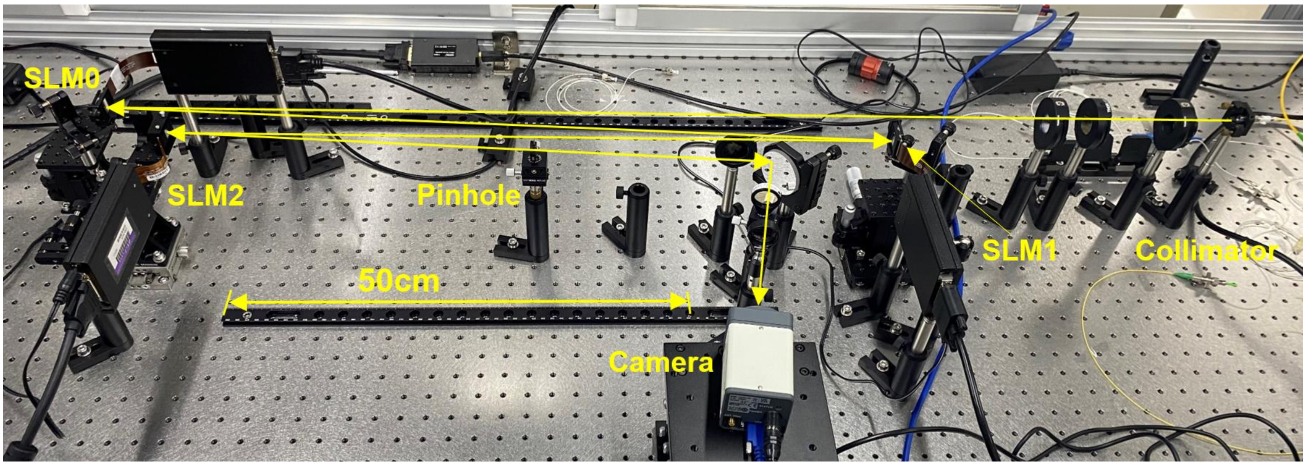

Supplementary Figure 2. The experimental setup.

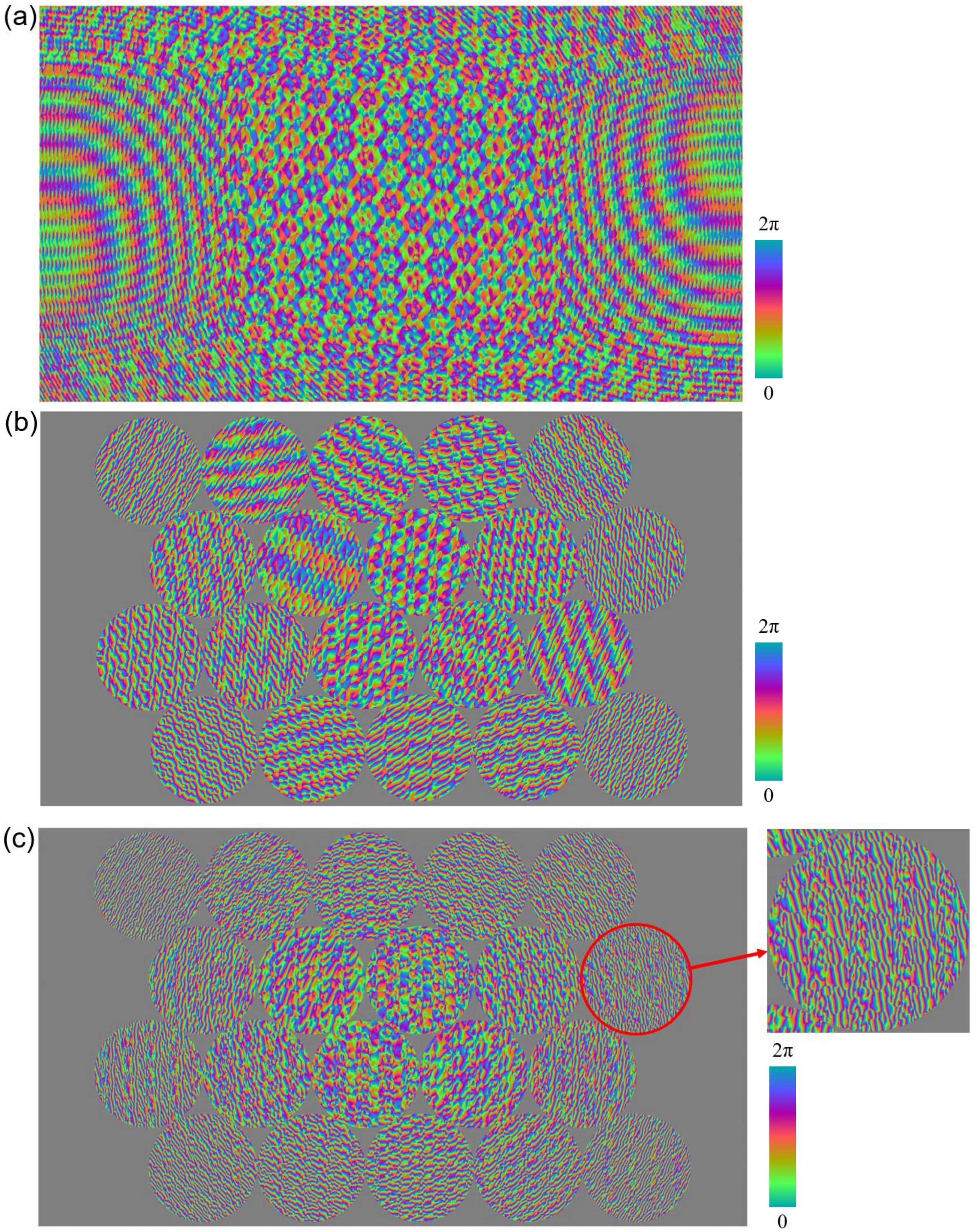

Supplementary Figure 3. The experimentally utilized phase patterns on spatial light modulators (SLMs) for model 2 (not superposed with the global blazed grating). (a) The beam-splitting pattern on SLM0. (b) The beam-splitting pattern on SLM1. (c) The beam-recombining pattern on SLM2. The inset shows a detailed beam-recombining region denoted by the red circle. The color bar indicates the phase value.

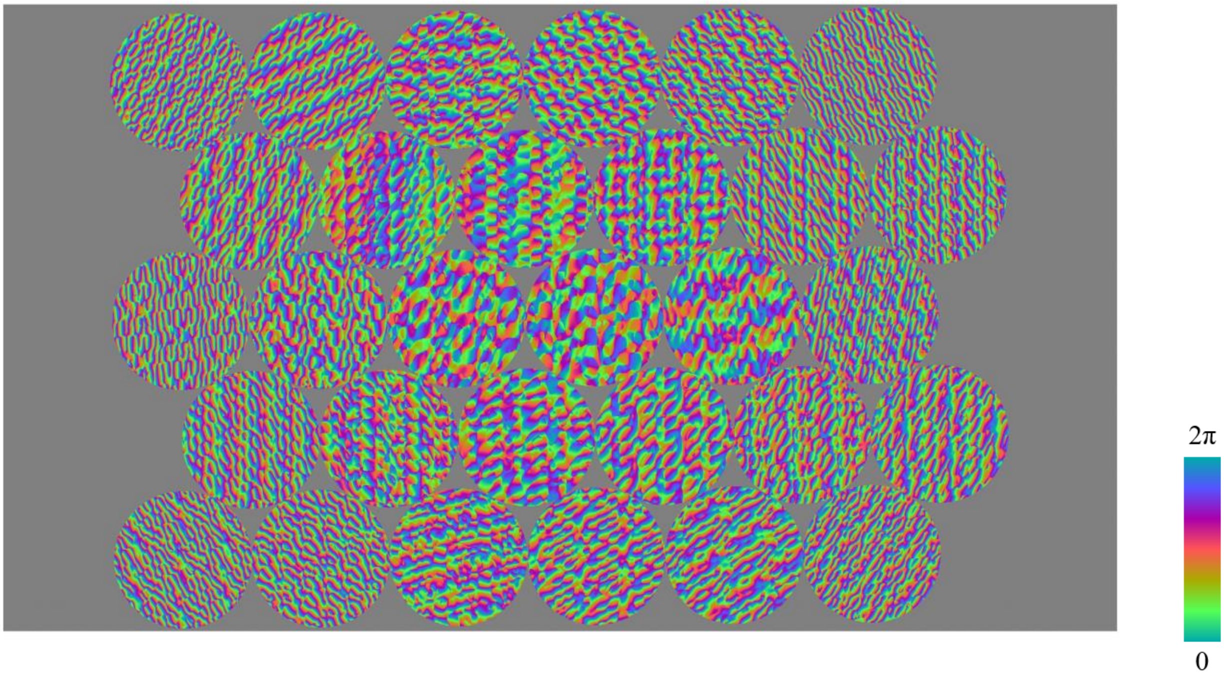

Supplementary Figure 4. The experimentally utilized beam-splitting phase pattern for model 3 (not superposed with the global blazed grating). The color bar indicates the phase value.

The method of generating phase patterns on SLMs. In our previous work[5,6], the method of generating the phase patterns on SLMs has been presented and the main procedure are described as follows. As mentioned in the main text, three SLMs are employed to generate the required beams, indexed SLM0, SLM1 and SLM2 respectively. SLM0 splits the incident beam into N beams, while SLM1 and SLM2 split and interweave the beams to perform multiplication and addition operations. The pixels outside the circular regions are filled with alternating 0 and π phase modulation according to the checkerboard method. Besides, as the employed SLMs are reflective, an additional global blazed grating with the period of 4 pixels is applied to each SLM pattern in order to concentrate the optical intensity in the first diffraction order. The beam from the collimator is centered at coordinate [0, 0] in the transverse xy plane. Then the beam is split and projected to N different circular regions on SLM1, as shown in Supplementary Figures 3b and 4. The ideal modulation function of SLM0 is the superposition of a series of blazed gratings[5,6]:

$$H_{\mathrm{SLM0,ideal}}(\mathbf{r}) = \sum_{n}^{N} \alpha_n \exp\left(\frac{-\mathrm{i}k}{L_{01}} \mathbf{r}_n \cdot \mathbf{r}\right), \tag{S8}$$

where $\mathbf{r}$ is the position vector in the xy plane, k is the wavenumber, $\mathbf{r}_n$ is the position vector of the center of the nth region of SLM1, α_n is the element of the input vector.

The ideal modulation function of nth circular region on SLM1 comprises two parts: a spin-encoding pattern and a beam-splitting pattern. The spin-encoding pattern just applies a phase delay of 0 or π to the beam according to its corresponding spin $\sigma_n = \pm 1$ and the beam-splitting pattern is a superposition of a lens mask and N blazed gratings[5,6]:

$$H_{\mathrm{SLM1,ideal},n}(\mathbf{r}) = \sigma_n \sum_{m=1}^{N} \beta_{mn} \exp\left[-\mathrm{i}k\left(\frac{\mathbf{R}_m - \mathbf{r}_n}{L_{12}} - \frac{\mathbf{r}_n}{L_{01}}\right) \cdot (\mathbf{r} - \mathbf{r}_n) + \theta_{mn}\right] \cdot H_{\mathrm{lens}}(\boldsymbol{r} - \boldsymbol{r}_n, f_1), \tag{S9}$$

$$H_{\mathrm{lens}}(\mathbf{r} - \mathbf{r}_n, f_1) = \exp\left(\mathrm{i}\frac{k|\mathbf{r} - \mathbf{r}_n|^2}{2f_1}\right), \tag{S10}$$

where β_{mn} is the element of the beam-splitting matrix, $\mathbf{R}_m$ is the position vector of the center of the mth region of SLM2, θ_{mn} is the phase compensation term due to different optical path, and H_{lens} is the phase modulation function of a lens. The lens with the focus f_1 adjusts the location of the beam waist to the middle of SLM1 and SLM2.

Each region on SLM2 recombines the N beams deflected by each region on SLM1 and a pinhole is set to filter out undesired light. The ideal modulation function of mth region on SLM2 is[5,6]

$$H_{\mathrm{SLM2,ideal},m}(\mathbf{r}) = \sum_{n=1}^{N} \gamma_{mn} \exp\left[-\mathrm{i}k\left(\frac{-\mathbf{r}_n}{L_{2\mathrm{p}}} - \frac{\mathbf{R}_m - \mathbf{r}_n}{L_{12}}\right)\cdot(\mathbf{r}-\mathbf{R}_m)\right] \cdot H_{\mathrm{lens}}(\mathbf{r}-\mathbf{R}_m, f_2), \tag{S11}$$

where γ_{mn} is the element of the beam-recombining matrix. The lens with the focus f_2 adjusts the location of the beam waist to the pinhole.

There is an evident caveat, however, that the ideal modulation functions above are not pure-phase, thus unattainable with the SLMs employed in our experiments. To address this issue, our previous work maps the value to a point on unit circle with the same argument[5,6]:

$$H_{\mathrm{SLM}}(\mathbf{r}) = \exp\{\mathrm{i}\arg[H_{\mathrm{SLM,ideal}}(\mathbf{r})]\} \tag{S12}$$

for it is the closest pure-phase solution to the original function in the sense of least squares. It is worth pointing out that this practice is empirical, and the errors for both the light field and the matrix elements would increase drastically with the dimensionality.

In this work, an improved iterative algorithm is employed to obtain the optimal phase-only patterns, which produce the light field distribution on the target plane approximating to an ideal distribution. The fundamental theory here is gradient descent. The main issue is how to optimize a real criterion function depending on complex-valued parameters. According to ref. [7], the optimizing theorems are handy to us.

(i) Preparations

The first step of optimization is to discretize the problem so that the computer processing can be performed. Consider a continuous model of light field propagation: light field given two parallel planes with aligned transverse coordinates, the propagation of the light field $u(x,y,0)$ on the first plane to the field $u(x',y',z_0)$ on the second plane can be described as[8]

$$u(x',y',z_0) = -u(x,y,0) \star \frac{1}{2\pi}\frac{\partial}{\partial z'}\left[\frac{e^{-\mathrm{i}kr}}{r}\right]_{z=z_0} = \mathrm{IFT}\left\{\mathrm{FT}\{u(x,y,0)\} \times \mathrm{FT}\left\{-\frac{1}{2\pi}\frac{\partial}{\partial z'}\left[\frac{e^{-\mathrm{i}kr}}{r}\right]_{z=z_0}\right\}\right\}, \tag{S13}$$

where $r = \sqrt{(x-x')^2 + (y-y')^2 + z^2}$, $\star$ denotes the convolution, and Fourier transform (FT) is utilized to compute the convolution.

Then the fields are sampled, and the Fourier transform and convolution are replaced with their discrete counterparts. For the sake of simplicity, the light fields are uniformly sampled in a rectangular area, aligned with both axes, and centered on the origin.

Let $\mathbf{H}_{z_0} \in \mathbb{C}^{3L_x \times 3L_y}$ denote the 2D-DFT of the respond $-\frac{1}{2\pi}\frac{\partial}{\partial z'}\left[\frac{e^{-\mathrm{i}kr}}{r}\right]_{z=z_0}$, and $\mathbf{U}, \mathbf{U}' \in \mathbb{C}^{L_x \times L_y}$ denote the sampling of light fields at $z=0$ and $z=z_0$, respectively. Noting the non-overlapping condition and the alignment of discrete convolution, the response has to be sampled from an area of double length in each dimension, then applied with $3L_x \times 3L_y$ 2D-DFT and finally clips the result to match the shape of $\mathbf{U}'$. To formulate it:

$$\mathbf{U}' = \mathrm{clip}\left(\mathrm{IDFT}_{3L_x,3L_y}\left(\mathrm{DFT}_{3L_x,3L_y}(\mathbf{U}) \odot \mathbf{H}_{z_0}\right)\Delta x \Delta y\right), \tag{S14}$$

where $\odot$ denotes element-wise multiplication, Δx and Δy denote the sampling interval along each axis, and $\mathrm{clip}(\cdot)$ clips extra zeros from the result matrix.

Now consider a surface at $z=0$, such as an SLM, and assume that each pixel independently produces a wavefront (rectangular, for example) proportional to their complex modulation coefficient. Let $\mathbf{M} \in \mathbb{C}^{3L_x \times 3L_y}$ denotes the 2D-DFT of the wavefront and $\mathbf{P} \in \mathbb{C}^{L_x \times L_y}$ denotes the coefficient matrix of the hologram. Now

$$\mathbf{U}' = \mathrm{clip}\left(\mathrm{IDFT}_{3L_x,3L_y}\left(\mathrm{DFT}_{3L_x,3L_y}(\mathbf{P}\odot\mathbf{U})\odot\mathbf{H}_{z_0}\odot\mathbf{M}\right)\Delta x\Delta y\right) = \mathbf{T}_{z_0}(\mathbf{P}\odot\mathbf{U}). \tag{S15}$$

Note that the composited operations are defined as $\mathbf{T}_{z_0}(\cdot)$, which is the discrete form of light field propagation function we desire.

(ii) Generate target light field

After discretization, a target light field is needed for each SLM to be optimized. A convenient approach is to treat the light field produced by ideal patterns as target. As well the initial values of optimization are such set with ideal patterns. To formulate it:

$$\mathbf{U}_\mathrm{T} = \mathbf{T}_{z_0}\left(H_{\mathrm{SLM,ideal}}\odot\mathbf{U}_\mathrm{I}\right), \tag{S16}$$

$$\mathbf{P}_0 = H_{\mathrm{SLM,ideal}}. \tag{S17}$$

(iii) Optimization steps

Given a target light field $\mathbf{U}_\mathrm{T}$ at $z=z_0$, an incident light field $\mathbf{U}_\mathrm{I}$ at $z=0$, and a hyperparameter δ, optimize phase pattern $\mathbf{P}$ in the sense (Huber Loss):

$$\begin{aligned}\mathrm{argmin}_{\boldsymbol{P}}\ \mathcal{L}(\mathbf{P};\mathbf{U}_\mathrm{T},\mathbf{U}_\mathrm{I},z_0,\delta) &= \sum_{i,j}\begin{cases}\frac{1}{2}\left|\mathbf{T}_{z_0}\left(\frac{\mathbf{P}}{|\mathbf{P}|}\odot\mathbf{U}_\mathrm{I}\right)-\mathbf{U}_\mathrm{T}\right|_{ij}^2, & \left|\mathbf{T}_{z_0}\left(\frac{\mathbf{P}}{|\mathbf{P}|}\odot\mathbf{U}_\mathrm{I}\right)-\mathbf{U}_\mathrm{T}\right|_{i,j}\le\delta\\ \delta\left|\mathbf{T}_{z_0}\left(\frac{\mathbf{P}}{|\mathbf{P}|}\odot\mathbf{U}_\mathrm{I}\right)-\mathbf{U}_\mathrm{T}\right|_{i,j}-\frac{1}{2}\delta^2, & \text{otherwise}\end{cases}\\ &= l\left(\mathbf{T}_{z_0}(\mathbf{N}(\mathbf{P}))\right),\end{aligned} \tag{S18}$$

where $\mathbf{T}_z(\cdot)$ is previously defined, $\left\{\begin{matrix}\cdot\\\cdot\end{matrix}\right.$ selects from two values and $\sum\cdot$ sums them up. Other operations here are all element-wise. Note that $l(\cdot)$ contracts the loss function and $\mathbf{N}(\mathbf{P})=\frac{\mathbf{P}}{|\mathbf{P}|}$ gives a phase-only hologram, which is what we eventually need.

Following the procedures described in ref. [7], we finally derive the gradient of $\mathcal{L}$ with respect to $\mathbf{P}$, which is:

$$\frac{\partial}{\partial\mathbf{P}^*}\mathcal{L} = \frac{1}{2}\mathbf{U}_\mathrm{I}\odot\left(-\frac{|\mathbf{P}|}{(\mathbf{P}^*)^2}\odot{\mathbf{T}'_{z_0}}^*\left(\frac{\partial}{\partial\mathbf{T}^*_{z_0}}l\right)+\frac{1}{|\mathbf{P}|}\odot\mathbf{T}'_{z_0}\left(\frac{\partial}{\partial\mathbf{T}^*_{z_0}}l\right)\right), \tag{S19}$$

where

$$\mathbf{T}'_{z_0}(\mathbf{Z}) = \mathrm{clip}\left(\mathrm{IDFT}_{3L_x,3L_y}\left(\mathrm{DFT}_{3L_x,3L_y}(\mathbf{Z})\odot\mathbf{H}^*_{z_0}\odot\mathbf{M}^*\right)\Delta x\Delta y\right). \tag{S20}$$

Finally, the gradient-descent-based algorithm is conducted to optimize the target phase-only hologram. Here is a sketch of the algorithm:

Input: target light field: $\mathbf{U}_\mathrm{T}$, incident light field: $\mathbf{U}_\mathrm{I}$, hyperparameter: δ, initial phase pattern: $\mathbf{P}$, iteration limit iter.
Output: $\mathbf{P}_\mathrm{o}$.
Initialization: optimizer: $\mathcal{O}\leftarrow\mathcal{O}_{\mathrm{RAdam}}$ (Rectified Adam Optimizer[9] is employed in our demonstration), loss function l: Huber loss.

$\mathbf{P}_0 = \mathbf{P}$

For $i = 1$ to iter do

Compute $\frac{\partial}{\partial\boldsymbol{P}^*_{i-1}}\mathcal{L}$

$\mathbf{P}_i = \mathcal{O}.\mathrm{step}\left(\frac{\partial}{\partial\boldsymbol{P}^*_{i-1}}\mathcal{L}\right)$

End for

Return $\mathbf{P}_{\mathrm{o}} = \frac{\mathbf{P}_{\mathrm{T}}}{|\mathbf{P}_{\mathrm{T}}|}$

Calibration method of the OVMM. Before the experiments, the whole system should be calibrated to achieve high fidelity of the implemented matrix transformation to reduce the systematic error. In the calibration stage, both the phase and amplitude terms are considered. The phase calibration method is improved from that used in our previous work[10].

Phase calibration. First, as mentioned above, the phase patterns of SLM1 and SLM2 are generated and set according to the all-one matrix. To measure the phase difference among the elements of the beam-splitting matrix, four output intensity matrices $\mathbf{M}_1$, $\mathbf{M}_2$, $\mathbf{M}_3$ and $\mathbf{M}_4$ have to be measured. In this section, each column of the input matrix would serve as the input vector one by one and the output matrix consists of the corresponding output vectors.

At first, the input matrix $\mathbf{m}_{\mathrm{in}}$ of SLM0 is defined as an $N \times (N-1)$ matrix with each column including two non-zero elements 1:

$$\mathbf{m}_{\mathrm{in}} = \begin{bmatrix} 1 & 1 & 1 & \dots & 1 \\ 1 & 0 & 0 & \dots & 0 \\ 0 & 1 & 0 & \dots & 0 \\ 0 & 0 & 1 & \dots & 0 \\ \vdots & \vdots & \vdots & \ddots & \vdots \\ 0 & 0 & 0 & \dots & 1 \end{bmatrix}. \tag{S21}$$

The process of phase calibration can be described as follows:

Initialization: input matrix: $\mathbf{m}_{\mathrm{in}}$, matrix on SLM1: all-one matrix, matrix on SLM2: all-one matrix.

For $\mathrm{i} = 1$ to $\mathrm{N} - 1$ do

Update SLM0 according to the column i of $\mathbf{m}_{\mathrm{in}}$

Measure the column i output intensity matrix $\mathbf{M}_1$

Deactivate the region $\mathrm{i} + 1$ of SLM1

Measure the column i output intensity matrix $\mathbf{M}_3$

Reset the SLM1 pattern

Deactivate the region 1 of SLM1

Measure the column i output intensity matrix $\mathbf{M}_4$

Reset the SLM1 pattern

Add the phase delay of $\pi/2$ to the region $\mathrm{i} + 1$ of SLM1

Measure the column i output intensity matrix $\mathbf{M}_2$

End for

Here, the operation "deactivate" refers to replacing a specific region with a "mirror" pattern where the phase modulation is uniform. Such pattern can reflect the incident beam away from the next SLM. Then how to use these matrices to conduct the phase calibration is introduced.

According to the process above, the interference intensities between the first and one of the rest of the beams have been measured as $\mathbf{M}_1$. Since none of the SLM patterns are calibrated, the actual input matrix can only be written as

$$\mathbf{m}'_{\mathrm{in}} = \begin{bmatrix} b_{11} & b_{12} & b_{13} & \dots & b_{1,N-1} \\ b_{21} & 0 & 0 & \dots & 0 \\ 0 & b_{32} & 0 & \dots & 0 \\ 0 & 0 & b_{43} & \dots & 0 \\ \vdots & \vdots & \vdots & \ddots & \vdots \\ 0 & 0 & 0 & \dots & b_{N,N-1} \end{bmatrix} \tag{S22}$$

The actual transformation matrix is denoted as $A'_{ij} = a_{ij} \exp(\mathrm{i}\varphi_{ij})$ so that the output amplitude matrix $\mathbf{m}_1 = \mathbf{A}'\mathbf{m}'_{\mathrm{in}}$ is

$$(m_1)_{ij} = a_{i1} b_{1j} \exp(\mathrm{i}\varphi_{i1}) + a_{i,j+1} b_{j+1,j} \exp(\mathrm{i}\varphi_{i,j+1}) \tag{S23}$$

and the corresponding measured output intensity matrix $\mathbf{M}_1$ is

$$(M_1)_{ij} = (m_1)^*_{ij}(m_1)_{ij} = a_{i1}^2 b_{1j}^2 + a_{i,j+1}^2 b_{j+1,j}^2 + 2a_{i1}b_{1j}a_{i,j+1}b_{j+1,j}\cos\left(\varphi_{i1} - \varphi_{i,j+1}\right). \tag{S24}$$

Similarly, the output amplitude matrix $\mathbf{m}_2$ is

$$(m_2)_{ij} = a_{i1}b_{1j}\exp(\mathrm{i}\varphi_{i1}) + a_{i,j+1}b_{j+1,j}\exp\left[\mathrm{i}(\varphi_{i,j+1} + \pi/2)\right] \tag{S25}$$

and the corresponding measured output intensity matrix $\mathbf{M}_2$ is

$$(M_2)_{ij} = (m_2)^*_{ij}(m_2)_{ij} = a_{i1}^2 b_{1j}^2 + a_{i,j+1}^2 b_{j+1,j}^2 + 2a_{i1}b_{1j}a_{i,j+1}b_{j+1,j}\sin\left(\varphi_{i1} - \varphi_{i,j+1}\right). \tag{S26}$$

Obviously, $(M_3)_{ij} = a_{i1}^2 b_{1j}^2$ and $(M_4)_{ij} = a_{i,j+1}^2 b_{j+1,j}^2$.

Therefore, the actual phase difference could be calculated according to

$$\Delta\varphi_{ij} = \varphi_{i1} - \varphi_{i,j+1} = \begin{cases} \arccos\left[\dfrac{(M_1)_{ij} - (M_3)_{ij} - (M_4)_{ij}}{2\sqrt{(M_3)_{ij}(M_4)_{ij}}}\right], (M_2)_{ij} - (M_3)_{ij} - (M_4)_{ij} \geq 0 \\ -\arccos\left[\dfrac{(M_1)_{ij} - (M_3)_{ij} - (M_4)_{ij}}{2\sqrt{(M_3)_{ij}(M_4)_{ij}}}\right], (M_2)_{ij} - (M_3)_{ij} - (M_4)_{ij} < 0 \end{cases}. \tag{S27}$$

It should be mentioned that Eq. (S27) can only calculate the phase differences among the elements in the same row. But this does not matter since the phase difference among different columns will not affect the output optical intensities. Finally, the phase-calibration matrix $\Delta\boldsymbol{\varphi}$ is obtained, and the input beam-splitting matrix of SLM1 is modified to $A_{ij}\exp(\mathrm{i}\Delta\varphi_{ij})$. It should be mentioned that such $\Delta\boldsymbol{\varphi}$ is independent to the transformation matrix and only determined by the optical setup so that it could be directly applied on other transformations.

Amplitude calibration. The process of the calibration of SLM1 can be described as follows.

Initialization: Input matrix: identity matrix, target transformation matrix: $\mathbf{A}$, beam-splitting matrix on SLM1: $(A_{\mathrm{SLM1}})_{ij} \leftarrow A_{ij}\exp(\mathrm{i}\Delta\varphi_{ij})$, pattern on SLM2: the same as that in phase calibration stage, repetition times: $n_{\mathrm{amp,1}}$.

For $i_{\mathrm{rep}} = 1$ to $n_{\mathrm{amp,1}}$ do

  Measure the output intensity matrix $\mathbf{C}$

  $(A_{\mathrm{SLM1}})_{ij} \leftarrow (A_{\mathrm{SLM1}})_{ij}\left|A_{ij}\right|/\sqrt{C_{ij}}$

  Generate and update the new phase pattern on SLM1 pattern according to $\mathbf{A}_{\mathrm{SLM1}}$

End for

In the 20/30-dimensional transformation, $n_{\mathrm{amp,1}} = 3\sim4$ is enough to obtain high fidelity. It should be mentioned that due to the phase-only operation, the SLM1 could only split the incident beams. Thus, the input vector of SLM0 has to be modified to compensate the difference between the beam-splitting matrix of SLM1 and the target matrix. Here, the actual contribution of each split beam from SLM0 to the output mode has to be measured. This can be achieved by activating each region of the calibrated SLM1 pattern successively (other regions are "deactivated" as mentioned above). The process is described as follows.

Initialization: target transformation matrix: $\mathbf{A}$, input vector of SLM0: $(E_{\mathrm{in}})_j \leftarrow \max_i\left(\left|A_{ij}\right|\right) / \sqrt{\max_i\left(C_{ij}\right)}$ ($\mathbf{C}$ is the last output intensity matrix in the amplitude calibration of SLM1), pattern on SLM1: calibrated pattern, SLM2 pattern: the same as that in phase calibration stage, repetition times $n_{\mathrm{amp,2}}$.

For $i_{\mathrm{rep}} = 1$ to $n_{\mathrm{amp,2}}$ do

  For $j = 1$ to N do

    Deactivate all regions except region j of SLM1

    Measure the output intensity vector $\mathbf{F}_j$

$$(E_{\mathrm{in}})_j \leftarrow (E_{\mathrm{in}})_j \max_i(|A_{ij}|) / \sqrt{\max_i(F_j)_i}.$$

End for

Generate and update the new SLM0 pattern according to $\mathbf{E}_{\mathrm{in}}$

End for

In the 20/30-dimensional condition, $n_{\mathrm{amp,2}} = 3{\sim}4$ is enough to obtain high fidelity.

In the end of this section, the 20-dimensional Discrete Fourier Transform (DFT) matrix is set as the target transformation to evaluate the calibration accuracy:

$$\mathbf{W} = \frac{1}{\sqrt{N}} \begin{bmatrix} 1 & 1 & 1 & \cdots & 1 \\ 1 & \omega & \omega^2 & \cdots & \omega^{N-1} \\ 1 & \omega^2 & \omega^4 & \cdots & \omega^{2(N-1)} \\ \vdots & \vdots & \vdots & \ddots & \vdots \\ 1 & \omega^{N-1} & \omega^{2(N-1)} & \cdots & \omega^{(N-1)(N-1)} \end{bmatrix}, \omega = e^{-\mathrm{i}\frac{2\pi}{N}}. \tag{S28}$$

Since the elements of both the DFT matrix and its inverse matrix have the same norms and only differ in arguments, it is very sensitive to the phase term. After the amplitude calibration of SLM1, the output intensity matrix corresponding to the input identity matrix is shown in Supplementary Figure 5a. It can be seen that each beam is equally split by SLM1, but the intensities in different columns are different. Then after the amplitude calibration of SLM0, the matrix $\mathbf{F}$ is shown as Supplementary Figure 5b, where the matrix elements are much closer to each other than that in Supplementary Figure 5a.

In order to evaluate the accuracy of the calibration, the input matrix is set as the inverse matrix of the DFT matrix, which is also the conjugate transpose. The output matrix should be the 20-dimensional identity matrix. Obviously, the input vector can be simply achieved by adding phase masks to each SLM1 region according to the arguments of the elements of the target input vector. The measured images are shown in Supplementary Figure 5d, where only one bright spot at different locations is observed in each image with similar intensities and high contrast. The output intensity matrix is shown as Supplementary Figure 5c where the intensity concentrates on the main diagonal elements. Here the fidelity f_{mat} is employed to evaluate the accuracy of the matrix transformation:

$$f_{\mathrm{mat}} = \frac{\sum_{ij}(I_{\mathrm{t}})_{ij}(I_{\mathrm{e}})_{ij}}{\sqrt{\sum_{ij}(I_{\mathrm{t}})_{ij}^2}\sqrt{\sum_{ij}(I_{\mathrm{e}})_{ij}^2}}, f_{\mathrm{mat}} \in [0,1] \tag{S29}$$

where $\mathbf{I}_{\mathrm{t}}$ is the theoretical output intensity matrix and $\mathbf{I}_{\mathrm{e}}$ is the experimentally measured intensity matrix. f_{mat} is normalized within [0,1]. In this demonstration, f_{mat} is calculated from the output intensity matrix in Supplementary Figure 5c and the identity matrix, resulting in a value as high as 0.99994.

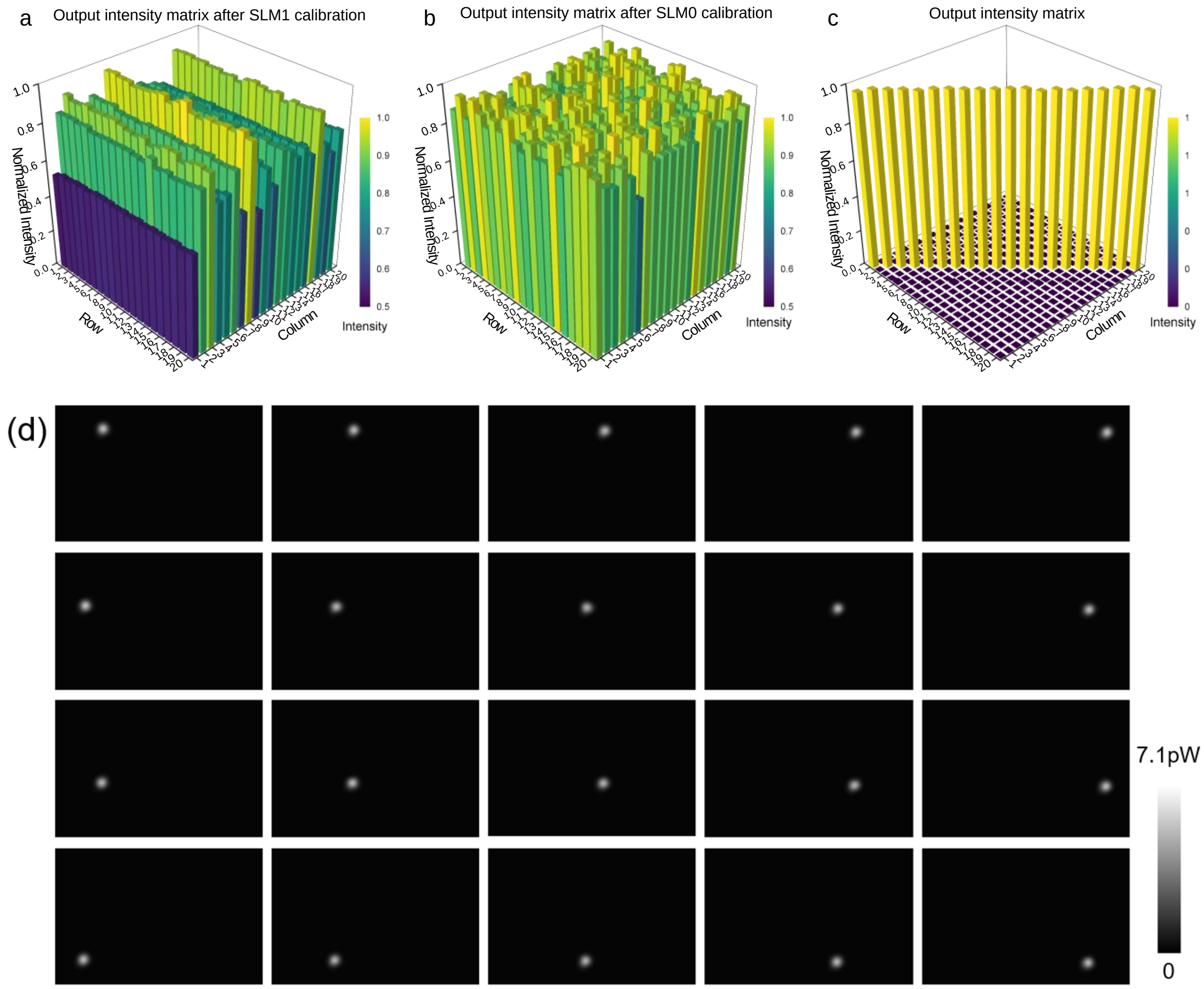

Supplementary Figure 5. The calibration of the Discrete Fourier Transformation matrix. (a) The output intensity matrix after the calibration of SLM1. (b) The output intensity matrix after the calibration of SLM0. (c) The output intensity matrix of the calibrated DFT matrix with the input matrix of its inverse matrix. (d) The measured images corresponding to each column in (c) respectively. The color bar denotes the incident power on each pixel.

Supplementary Note 4: The fidelities of different transformation matrices

In Supplementary Note 3, the results of the 20-dimensional DFT matrix have verified the validity of our OVMM system. In this section the fidelities of the three matrix transformations of model 1-3 are discussed. Since their inverse matrices usually do not consist of the column vectors with equal norms like DFT matrices, here the output intensity matrices corresponding to the calibrated input identity matrices (like Supplementary Figure 5b) are used to evaluate the transformation fidelities. The results are shown in Supplementary Figure 6. It can be seen that the two matrices are very similar in each model. The fidelities of the intensity matrices are 0.9989, 0.9994, and 0.9969 for model 1-3 respectively. Such results indicate that our OVMM system is also capable of achieving the matrices with highly different elements.

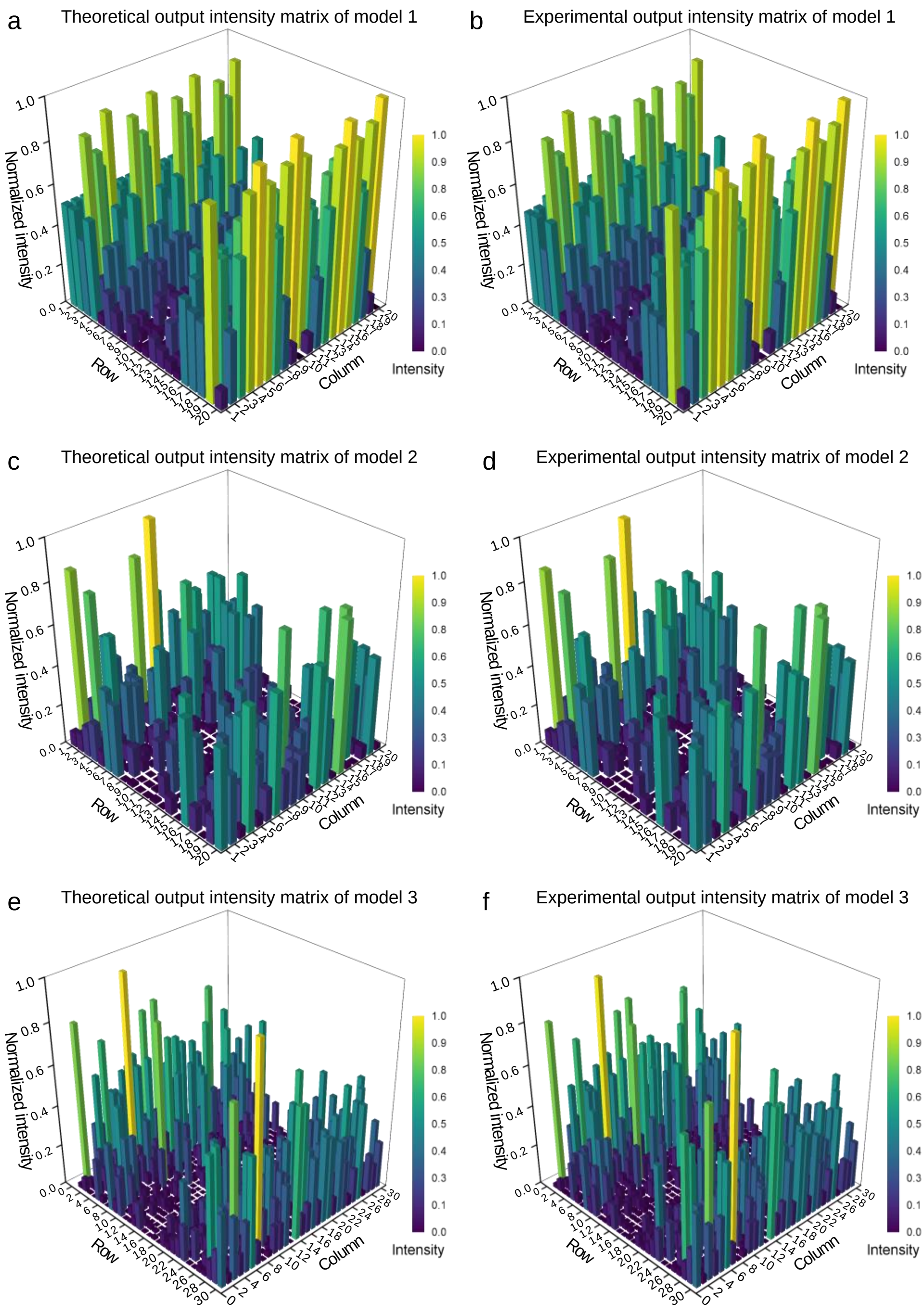

Supplementary Figure 6. The comparison of the normalized theoretical and experimental output intensity matrices for model 1-3. (a) (b) The results of model 1. (c) (d) The results of model 2. (e) (f) The results of model 3.

Supplementary Note 5: The accuracy of the output intensity vectors

Besides the matrix fidelity, the accuracy of the output vectors also needs to be investigated since the output vectors are directly corresponding to the Hamiltonians. Here, the accuracy of the output vectors is evaluated with two parameters.

According to the main text, there should be a constant normalization coefficient $K = H_{\mathrm{exp}}/H_{\mathrm{theo}}$ (samples with $H_{\mathrm{theo}} = 0$ are excluded) between the theoretical Hamiltonian and the experimental Hamiltonian, which is the first parameter representing the accuracy of the norm of the output intensity vector. The 100 raw experimental Hamiltonian evolution curves obtained from the captured images of model 1-3 are shown in Supplementary Figures 7a-7c respectively. Actually, the target of the PEIDIA is to obtain the spin vector of the ground state, rather than the actual value of the

Hamiltonian. Thus, the accepted spin vectors in each iteration corresponding to all curves in Supplementary Figures 7a-7c are extracted to calculate the theoretical Hamiltonians with Eq. (1) in the main text for model 1-3, and the results are shown in Supplementary Figures 7d-7f respectively. From Supplementary Figures 7d-7f it can be seen that most curves converge to the ground state Hamiltonians denoted by the black dashed lines (H_{min}=-26, -62, -117 for model 1-3 respectively) in the end, but their corresponding experimental Hamiltonians are distributed within a small range. To find out the reason, the average value of K of each run of model 1-3 is calculated according to H_{exp} and H_{theo} of the actually sampled states rather than the accepted states, and the results are shown in Supplementary Figures 7g-7i respectively. The variation of K in each run is mainly resulted from the detection noise, which will be discussed in detail in Supplementary Note 6. Each experimental Hamiltonian evolution curve is normalized with its own average value of K, and the results are shown in Supplementary Figures 7j-7l and for model 1-3 respectively. Such results indicate that our OVMM system possesses relatively high accuracy.

The second parameter is the fidelity f_{vec} of the output intensity vector, which is defined as

$$f_{\mathrm{vec}} = \frac{\sum_i \left(I_{\mathrm{exp}}\right)_i \left(I_{\mathrm{theo}}\right)_i}{\sqrt{\sum_i \left(I_{\mathrm{exp}}\right)_i^2 \sum_i \left(I_{\mathrm{theo}}\right)_i^2}}, f_{\mathrm{vec}} \in [0,1], \tag{S30}$$

where $\mathbf{I}_{\mathrm{exp}}$ and $\mathbf{I}_{\mathrm{theo}}$ denote the experimental and theoretical output intensity vectors, respectively. Such fidelity represents the parallelism between the two vectors. In the main text, the vector fidelities of model 1-3 have been discussed with the high average values of 0.99978±0. 00039, 0.99976±0.00044 and 0.99942±0.00131, respectively. Besides, the time stability of the fidelity is also investigated. Supplementary Figure 8 shows the average fidelity of each run of model 1-3 respectively. It can be seen that there is no obvious deterioration of the average fidelities, indicating that our OVMM system is quite stable.

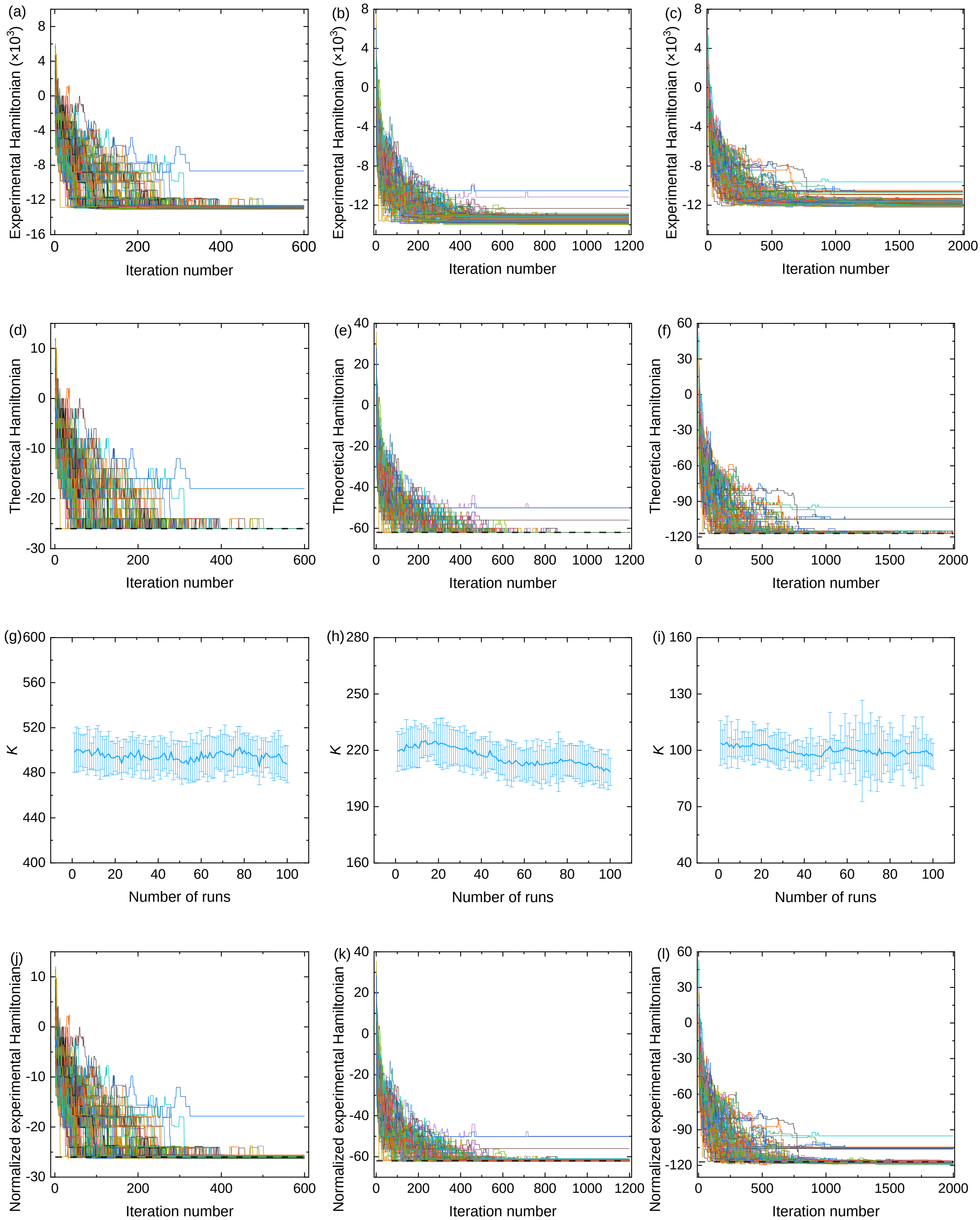

Supplementary Figure 7. Results of the ground state search of model 1-3. (a)-(c) The experimental Hamiltonian curves of model 1-3 respectively, which are calculated according to Eq. (S7). (d)-(f) The theoretical Hamiltonian curves corresponding to (a)-(c) respectively. (g)-(i) The average value of K of each run of model 1-3 respectively. The error bar denotes the standard deviation. (j)-(l) The normalized experimental Hamiltonian curves of model 1-3 respectively.

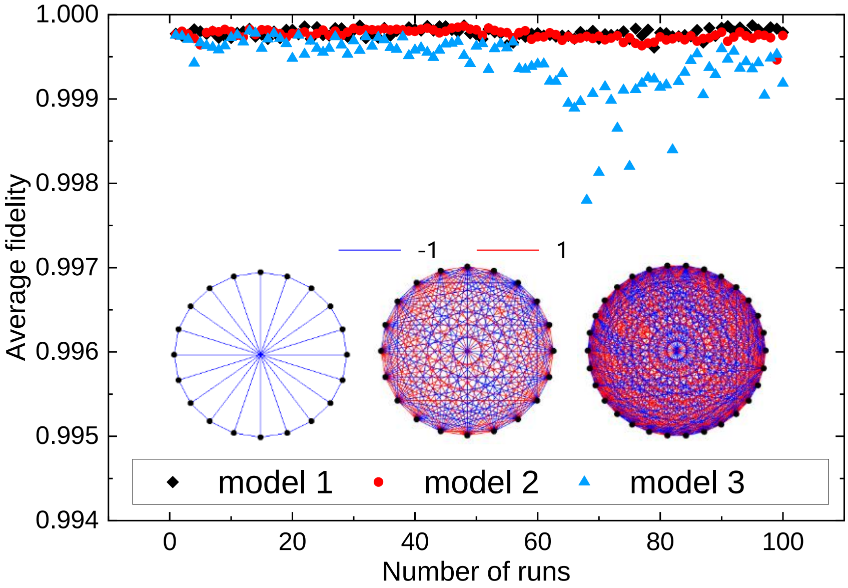

Supplementary Figure 8. The average fidelities of 100 runs of model 1-3. The inset shows the corresponding Ising models.

Supplementary Note 6: The error analysis and the searching accuracy of the experimental Hamiltonians

Though high transformation fidelities have been achieved in the experiment, the measurement error of the experimental Hamiltonians should be investigated further. According to the experimental results shown in Supplementary Note 4 and 5, the systematic error has been well compensated by the calibration. Thus, we will mainly discuss the random error of measuring Hamiltonians in this section. From Eq. (S7) we have

$$H_{\mathrm{exp}} = \frac{1}{2}\left(\sum_{i,\lambda_i<0} I_i - \sum_{i,\lambda_i>0} I_i\right), \tag{S31}$$

where H_{exp} is the experimental Hamiltonian, and I_i is the measured intensity of each beam. The uncertainty of H_{exp} is

$$\delta_H^2 = \sum_{i=1}^{N}\left(\frac{\partial H_{\mathrm{exp}}}{\partial I_i}\right)^2 \delta_{I_i}^2 = \frac{1}{4}\sum_{i=1}^{N}\delta_{I_i}^2 \tag{S32}$$

where N is the number of detectors, as well as the optical beams. Here, we assume that the uncertainties introduced by different detectors are independent. The PEIDIA is placed on an optical table with vibration isolators and covered by a glass cabinet, while the temperature of the whole laboratory is kept constant. Besides, the camera has a forced air-cooling system to maintain the operating temperature at 10°C. Thus, it is reasonable to neglect the convection and the drift noise in the experiment, and the uncertainty of each I_i is mainly introduced by the noise of the detector. For the employed Hamamatsu C12741-03 camera, the noise of each pixel δ_{I_i} mainly consists of 3 independent parts: the readout noise δ_{r} (including the thermal noise and the quantization noise δ_{q}), the dark noise δ_{d} and the photon shot noise $\delta_{\mathrm{p_i}}$:

$$\delta_{I_i}^2 = \delta_{\mathrm{r}}^2 + \delta_{\mathrm{d}}^2 + \delta_{\mathrm{p_i}}^2. \tag{S33}$$

It should be mentioned that the photon shot noise $\delta_{\mathrm{p_i}}$ of each pixel is equivalent to the square root of the signal. The noises can be inferred from the parameters in the datasheet of the camera which are listed in Supplementary Table 1:

Parameter	Symbol	Value	Unit
Full well capacity	C_{well}	6×10^5	electron
Number of bits of the analog-to-digital converter	B_{ADC}	14	bit
Dark current* (under cooling temperature 10°C)	i_{d}	60	fA
Exposure time of a frame	Δt	16.7	ms
Maximum readout noise	δ_{r}	1000	electron

Supplementary Table 1. The parameters necessary for the noise evaluation. The dark current marked by star is referred from Hamamatsu InGaAs camera G14671-0808W as it is not provided in the datasheet of C12741-03.

In the datasheet, the number of excited electrons per pixel per frame is employed to evaluate the readout noise. Thus, we use the same unit to analysis other noises instead of the common unit of power. Using the parameters in Supplementary Table 1, the noises can be evaluated and listed in Supplementary Table 2.

Noise type	Symbol	Expression	Value (electron)
Quantization noise	δ_{q}	$\dfrac{C_{\mathrm{well}}}{2^{B_{\mathrm{ADC}}-1}}\cdot\dfrac{1}{\sqrt{12}}$	21
Dark noise	δ_{d}	$\sqrt{i_{\mathrm{d}}\Delta t/e}$	79
Maximum photon shot noise	δ_{p}	$\sqrt{C_{\mathrm{well}}}$	774

Supplementary Table 2. The expressions and the corresponding values of different types of noise. e=1.6×10^{-19}C is the elementary charge.

It is necessary to investigate the noise level of the ground state, which is our main concern. From the experimentally measured ground state signals of model 1-3 shown in Supplementary Figure 9, it can be found that the signals most concentrates on the last beams respectively.

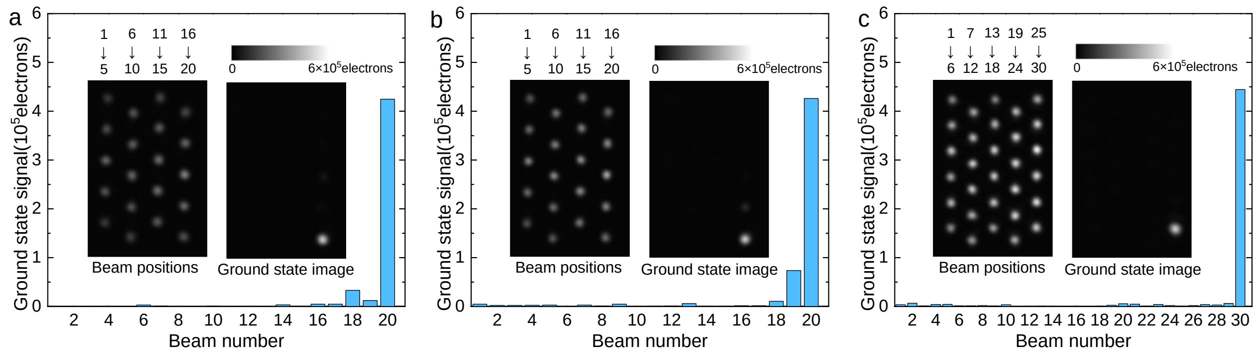

Supplementary Figure 9. Experimentally measured ground state signals of model 1-3. (a)-(c) correspond to model 1-3 respectively. The left insets denote the beam positions while the right insets show the ground state images, respectively. The color bar denotes the signal intensity of each pixel in the images.

Thus, we can take a rough approximation of the output signal corresponding to the Ising ground state: the detected signals of beam 1 to N-1 are 0 while the signal of beam N is the maximum value C_{well}. The corresponding experimental ground state Hamiltonian is H_0=-3×10^{5}electrons according to Eq. (S31). Thus, the photon shot noises of beam 1 to N-1 $\delta_{\mathrm{p}_1}, \delta_{\mathrm{p}_2}, \dots, \delta_{\mathrm{p}_{N-1}}$ are 0 while that of beam N is $\delta_{\mathrm{p}_N} = \sqrt{C_{\mathrm{well}}}$ =774electrons. Therefore, the total noises of beam 1 to N-1 are $\delta_{I_1} = \delta_{I_2} = \cdots = \delta_{I_{N-1}} = \sqrt{\delta_{\mathrm{r}}^2 + \delta_{\mathrm{d}}^2} \approx$ 1003electrons, and that of beam N is $\delta_{I_N} = \sqrt{\delta_{\mathrm{r}}^2 + \delta_{\mathrm{d}}^2 + \delta_{\mathrm{p}_N}^2} \approx$ 1267electrons. It can be found that the major noise of the whole system is the readout noise of the detector. Then we obtain the uncertainty of the experimental ground state Hamiltonian as

$$\delta_H = \frac{1}{2}\left[(N-1)\delta_{I_1}^2 + \delta_{I_N}^2\right]^{\frac{1}{2}} . \tag{S34}$$

Eq. (S34) indicates that δ_{H} is approximately proportional to $\sqrt{N}$. Moreover, now the signal-to-noise ratio (SNR) of the experimental ground state Hamiltonians can be estimated as $|H_0/\delta_H|$, which are shown in Supplementary Table 3.

Dimensionality N	δ_H (electron)	SNR=20log$\lvert H_0/\delta_H \rvert$ (dB)
20 (model 1 and 2)	2276	42.4
30 (model 3)	2774	40.7

Supplementary Table 3. The signal-to-noise ratios of the experimental ground state Hamiltonians. H_0=-3×10^{5}electrons.

Furthermore, to quantify the influence of the noise during the ground state search, it is reasonable to investigate the "resolution" of the Hamiltonian, which evaluates the searching accuracy of the PEIDIA. An intuitional conclusion is that the PEIDIA cannot distinguish two states if the difference of measured Hamiltonians is less than the noise level. In this discussion, we use the ground state noise level δ_H to represent the noise level of other spin states as a reasonable approximation. Then we define the resolution of the Hamiltonian by $R = |\delta_H/H_0|$. Besides, we can define the relative Hamiltonian interval ΔH_{r} of two states by the ratio of the difference of the theoretical Hamiltonians ΔH_{theo} to the minimum theoretical Hamiltonian H_{min} as $\Delta H_{\mathrm{r}} = |\Delta H_{\mathrm{theo}}/H_{\mathrm{min}}|$. For instance, in model 1-3 the interaction strength $|J_{ij}|$=1. Thus, when only one spin flips, the absolute value of the minimum Hamiltonian variation is 2. Then we obtain the results shown in Supplementary Table 4:

Parameter	Model 1	Model 2	Model 3
Minimum theoretical Hamiltonian H_{min}	-26	-62	-117
Minimum relative Hamiltonian interval ΔH_{r}	7.69×10^{-2}	3.22×10^{-2}	1.71×10^{-2}
Resolution of the Hamiltonian R	7.59×10^{-3}	7.59×10^{-3}	9.25×10^{-3}

Supplementary Table 4. The parameters for evaluating the searching accuracy in the experiment of model 1-3.

According to Supplementary Table 4, all ΔH_{r} are larger than R in model 1-3, which indicates that the PEIDIA can well distinguish two states with minimum Hamiltonian interval in model 1-3. Such result is consistent with the achieved high ground state probability in our experiments. The above analysis indicates that the performance of ground state search significantly depends on the Hamiltonian landscape of the given Ising model. The resolution of the Hamiltonian is relative to the dimensionality with the approximation of $R{\sim}\sqrt{N}$, which indicates the possible deterioration of the searching accuracy in high-dimensional Ising problems. Another interesting conclusion is that although the SNR of H_{exp} becomes extremely low when H_{exp}~0, the PEIDIA can still distinguish different spin states around H_{exp}~0 since the searching accuracy is only determined by the resolution of the Hamiltonian.

In conclusion, the major noise of the whole system is the readout noise of the detector and the SNR of the ground state Hamiltonian would decrease according to $\sim 1/\sqrt{N}$ with increasing dimensionality N, which would be one of the challenges to expand the dimensionality of the PEIDIA.

Supplementary Note 7: Operation speed and energy consumption

The time cost per iteration t_{iter} in optical domain depends on the propagation time of light t_{p}, the updating time of the SLM1 t_{u} and the detection time of the camera t_{d}. The distance between the SLM1 and the camera is ~1.5m in the experiment, hence in a single iteration, t_{p}=5ns. Although the updating of the new SLM1 pattern only needs appending a phase delay mask to the old one, it still requires matrix operations with dimensionality of 1920×1080 (same as the SLM resolution), which takes about t_{u}=0.15s. Likewise, the transmission and processing of the image (resolution of 230×340) take about t_{d}=0.17s, while only intensities of N pixels at beam centers are needed. Hence the time cost in the optical domain per iteration is $t_{\mathrm{o}} = t_{\mathrm{p}} + t_{\mathrm{u}} + t_{\mathrm{d}}$≈0.32s. The time cost t_{e} of the rest operations of an iteration in the electronic domain is much less than t_{o} and is negligible. Thus, the total time cost per iteration is t_{iter}≈0.32s. In each iteration, the OVMM can perform $F = 2N^2 + 2N$ floating-point operations (FLOPs)[11], including $2N^2$ multiplications of $\mathbf{A\sigma}$ and $2N$ multiplications of the element-wise product of the output amplitude vector in the complex field. Take model 3 as an example, for N=30, the operation speed of the OVMM is $R = F/t_{\mathrm{iter}}$ =5.81kFLOP/s.

In the experimental demonstration, the power of the input laser is about 2.59μW, 2.07μW and 6.01μW for model 1-3 respectively. The energy consumption mainly depends on the sensitivity of the camera in our current demonstration. With the employed camera, the laser power of P_{l}=6μW is able to achieve high enough signal-to-noise ratio in the experiment of model 3, and the maximum power of the camera is P_{c} =16W. Thus, the energy consumption is $e_{ff} = (P_{\mathrm{l}} + P_{\mathrm{c}})/R$ =2.75mJ/FLOP.

Symbol	Description
$\boldsymbol{\sigma}/\sigma_i$	Ising spin vector/ith Ising spin
H	Ising Hamiltonian
N	Number of spins in an Ising model
$\mathbf{J}/J_{ij}$	Ising adjacent interaction matrix/element of $\mathbf{J}$
$\mathbf{J}_+$	The symmetric component of $\mathbf{J}$
$\mathbf{J}_-$	Anti-symmetric component of $\mathbf{J}$
$\mathbf{Q}$	Normalized orthogonal eigenvector matrix of $\mathbf{J}$
$\mathbf{D}$	Diagonal eigenvalue matrix of $\mathbf{J}$
λ_i	ith eigenvalue of $\mathbf{J}$
$\mathbf{A}$	$\mathbf{A} = \sqrt{\mathbf{D}}\mathbf{Q}$, the transformation matrix in the OVMM
$\mathbf{E}/E_i$	Output complex amplitude vector /ith element of $\mathbf{E}$
E_0	Constant amplitude term of the output field
φ_0	Constant phase term of the output field
φ_i	ith phase term relative to φ_0
$\mathbf{I}/I_i$	Output intensity vector/ith output intensity
Superscript $\star^{(n)}$	Certain parameter $\star$ in iteration n
α	Cauchy scaling coefficient
T	Annealing temperature
ΔH	Hamiltonian variation of two adjacent iteration
f	Fidelity of the output intensity vector
$\mathbf{I}_{\text{theo}}$	Ideal output intensity vector
w	Radius of the Gaussian beam
w_0	Radius of beam waist between SLM1 and SLM2
λ	Wavelength of beam
z	Axial distance relative to beam waist
z_{SLM}	Half of the distance between SLM1 and SLM2
w_{SLM}	Minimum beam radius on SLM1 and SLM2
$t_{\text{o}}/t_{\text{e}}$	Time cost on optical/electronic domain per iteration
t_{p}	Propagation time of light per iteration
t_{u}	Updating time of SLM1 per iteration
t_{d}	Detection time of camera per iteration
F	FLOPs of OVMM per iteration
R	Operation speed of OVMM
t_{iter}	Total time cost per iteration
P	Total energy consumption of the optical system
e_{ff}	Energy consumption per FLOP
$(T_0)_{\text{exp}}/(T_0)_{\text{simu}}$	Initial annealing temperature in the experiment/simulation
$n_{\text{step}}/n_{\text{temp}}$	Steps per temperature stage/Stages of temperature
η	Annealing coefficient
K	Normalization coefficient of the experimental Hamiltonian

Supplementary Table 5. Descriptions of the symbols in the main text.

Supplementary References:

1. Abdi, H. The eigen-decomposition: Eigenvalues and eigenvectors. *Encyclopedia of measurement and statistics* 304–308 (2007).
2. Kirkpatrick, S., Gelatt Jr, C. D. & Vecchi, M. P. Optimization by simulated annealing. *science* **220**, 671–680 (1983).
3. Van Laarhoven, P. J. & Aarts, E. H. Simulated annealing. in *Simulated annealing: Theory and applications* 7–15 (Springer, 1987).
4. Ingber, L. & Rosen, B. Genetic Algorithms and Very Fast Simulated Reannealing: A comparison. *Mathematical and Computer Modelling* **16**, 87–100 (1992).
5. Wang, Y., Potoček, V., Barnett, S. M. & Feng, X. Programmable holographic technique for implementing unitary and nonunitary transformations. *Physical Review A* **95**, 033827 (2017).
6. Zhao, P. *et al.* Universal linear optical operations on discrete phase-coherent spatial modes with a fixed and non-cascaded setup. *Journal of Optics* **21**, 104003 (2019).
7. Hjorungnes, A. & Gesbert, D. Complex-valued matrix differentiation: Techniques and key results. *IEEE Transactions on Signal Processing* **55**, 2740–2746 (2007).
8. Delen, N. & Hooker, B. Free-space beam propagation between arbitrarily oriented planes based on full diffraction theory: a fast Fourier transform approach. *JOSA A* **15**, 857–867 (1998).
9. Liu, L. *et al.* On the variance of the adaptive learning rate and beyond. *arXiv preprint arXiv:1908.03265* (2019).
10. Li, S. *et al.* Programmable coherent linear quantum operations with high-dimensional optical spatial modes. *Physical Review Applied* **14**, 024027 (2020).
11. Shen, Y. *et al.* Deep learning with coherent nanophotonic circuits. *Nature Photon* **11**, 441–446 (2017).